2020 IEEE/RSJ International Conference on Intelligent Robots and Systems (IROS)
October 25-29, 2020, Las Vegas, NV, USA (Virtual)

PresSense: Passive Respiration Sensing via Ambient WiFi Signals in Noisy Environments

Yi Tian Xu, Xi Chen, Xue Liu, David Meger, and Gregory Dudek

***Abstract*— Passive sensing with ambient WiFi signals is a promising technique that will enable new types of human-robot interactions while preserving users' privacy. Here, we present PresSense, a system for human respiration sensing in noisy environments. Unlike existing WiFi-based respiration sensors, we employ a human presence detector, improving the robustness in scenarios where no human is present in an Area Of Interest (AOI). We also integrate our novel feature, Peak Distance Histogram (PDH), with other classic WiFi features to achieve better accuracy when someone is present in the AOI. We tested our system using commodity WiFi devices in an office room. Our PresSense outperforms the state of the arts in both respiration rate estimation and presence detection.**

I. Introduction

To enable robots to sense the surrounding environment, numerous types of sensors have been developed, including ranging sensors [1], [2], haptic sensors [3], proximity sensors [4] and inertial sensors [5]. In this paper, we explore the potential of commodity WiFi devices as a type of passive sensor for detecting human presence and respiration rates. In fact, WiFi sensing has been used for localization of humans [6], [7] and robots [8], pinpointing personal devices [9], trajectory tracking [10] and activity recognition [11]. With the ability to cover a wide area and to penetrate through objects and walls, it can provide a cost-effective and low-power sensing solution. In particular, passive WiFi sensing may also offer a new approach for human-robot interactions with its ubiquitousness and privacy-preserving ability, providing the autonomous agent with the awareness of the human's presence, state of activity and location, without using intrusive sensors such as cameras and LiDARs.

Mounting a WiFi sensor on the robot will allow it to "hear" patterns in the WiFi signals. These patterns generally come from environment changes or moving objects that cause distortions in the multipath propagation of WiFi signals. In particular, the regular motion of a human chest during respiration causes a regular shortening and lengthening in the paths reflected from the chest to the receiver. This can be recovered as a periodic pattern in the received signals (see Figure 1). Unlike large motions, such as walking or waving, which can be effectively detected using a decision threshold [6], the subtle respiration of a stationary human can be easily confounded with background noise. A series of advances in sensing with commodity WiFi devices has developed various techniques to accurately estimate the respiration rate across arbitrary locations of the human body

The authors are with Samsung AI Center, Montreal, Quebec, Canada. {yitian.xu, alex.chen1, steve.liu, greg.dudek}@samsung.com, david.meger@partner.samsung.com

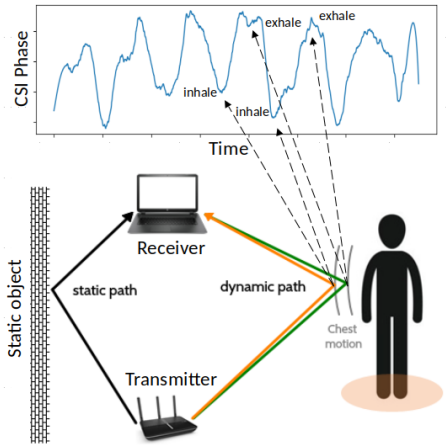

Fig. 1: An example of a WiFi propagation path reflected off the human chest during respiration, causing a periodic pattern in the measured WiFi signal (CSI phase).

for smart home and hospital environments [12]–[21]. Recent work has also pushed the sensing range up to house level (8-9 meters) [22].

The existing systems estimate the respiration rate based on the peak/valley distances in the detected periodic patterns with strong signal strength. However, they operate under the scenarios where there is one and only one person in the entire sensing area. Realistic scenarios may involve several people outside of an Area Of Interest (AOI) conflicting with the respiration signal of interest, or acting as impostors in an empty AOI. We further improve the single-person scenario with a novel WiFi feature, Peak Distance Histogram (PDH), which captures the occurrence of periodic patterns in the received signal. Then, using respiration as an intrinsic indicator of human presence and vice-versa, we extend the system to realistic scenarios by combining presence detection and respiration sensing. Our system, PresSense, uses respiration information extracted from PDH in concert with other existing features and learns a Respiration rate selector and a presence detector. The latter is used to confirm the existence of a valid respiration, and thus avoid to detect a "ghost breather" in an empty AOI. Our solution demonstrates improved accuracy and robustness for both presence detection and respiration sensing.

In summary, our contributions are twofold:

- We propose the design of a passive WiFi sensing system, PresSense, that outperforms the state of the arts in both presence detection and respiration rate estimation.

- We present a novel WiFi feature, Peak Distance Histogram (PDH), capturing the occurrence of periodic patterns in the signal. Our experiment demonstrates the improved accuracy in the aforementioned tasks when the feature is used in PresSense.

II. Background

WiFi sensing has been proved as a promising technique in various applications, including identifying users [23] and estimating respiration rates [22]. More importantly, the above missions can be accomplished in a device-free manner, meaning that users are not required to carry any devices. To achieve this, instead of using classic triangulation-like methods, a WiFi sensing system extracts the distortions that humans cause on the ambient WiFi signals, and learns the association between these distortions and human information (e.g., locations, activities and respiration rates).

To see how this can be achieved, we next present some necessary background on WiFi standards and Channel State Information (CSI). According to the IEEE 802.11n standards [24], a WiFi channel is divided into 64 subcarriers using the Orthogonal Frequency-Division Multiplexing (OFDM) technology. Every subcarrier can carry one data symbol. Two adjacent subcarriers are overlapping (50%) and orthogonal with each other, as illustrated in Fig. 2(a). In this way, more subcarriers can be placed into a limited bandwidth, and thus more data can be transmitted. In addition, WiFi supports spatial multiplexing, where different data can be transmitted on different spatial streams, as illustrated in Fig. 2(b). A spatial stream, or stream for short, is the signal flow between a transmission antenna and a receiving antenna.

The WiFi CSI describes how the WiFi signal propagates on the subcarriers through these streams. Denote the complex data signal transmitted on the ith subcarrier and the jth stream as $a_{i,j}$, and denote the corresponding received signal as $b_{i,j}$. The received signal $b_{i,j}$ is basically the transmitted signal $a_{i,j}$ altered by the WiFi channel, i.e.,

$$b_{i,j} = h_{i,j} \cdot a_{i,j}, \tag{1}$$

where $h_{i,j}$ is the complex-value CSI.

The value of a CSI can be affected by every object in between the transmitter and the receiver, and is very sensitive to small movements like human respiration. For example, in Fig. 1, by looking at the phases of CSI, we can find some periodic patterns corresponding to inhalations and exhalations. A straightforward solution would be running peak/valley detection algorithms on the CSI phases and extracting the intervals between peaks/valleys as the respiration periods. However, in the real scenarios, the CSI readings could be much noisier than those in the above example. Moreover, the changes caused by respiration could be easily overwhelmed by other human movements and by unobservable phase offsets introduced by the hardware.

III. Design

We consider the case when the AOI is an office with several people sitting and walking nearby, and that it can either be empty or occupied by one person with a stationary posture. PresSense estimates the underlying states of the AOI (i.e.: occupied or empty, and the respiration rate if occupied) conditioned on the measurable WiFi signals of $n_s = 2$ streams and n_x subcarriers over a period of time. We consider that normal respiration ranges between 10 to 37 breaths per minute (bpm) [13]. The architecture of PresSense is illustrated in Fig. 3.

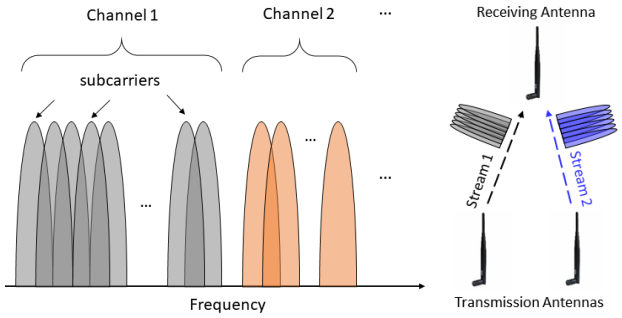

(a) WiFi frequency subcarriers. (b) WiFi streams.

Fig. 2: WiFi frequency and spatial multiplexing.

Upon observing a sequence of $n \in \mathbb{N}^*$ CSI measurements,

$$X = (H[1], H[2], \ldots, H[n]), \tag{2}$$

where each $H[t]$ denotes a complex CSI matrix of dimension $n_x \times n_s$ collected at time $t \in \{1, \ldots, n\}$, the measurements are first passed through a CSI Cleanser module for phase offsets and noise filtering. The subsequent Feature Extractor extracts relevant features for presence and respiration rate sensing, combining existing WiFi features with our PDH. A portion of the features is passed to a leaning model for binary classification. Another overlapping portion is passed to our Respiration Rate Selector module to select our best rate estimate according to the amount of noise in the environment. Finally, if human presence is detected, our selected rate estimate will be outputted.

A. CSI Cleanser

Currently, we are aware of no techniques to perfectly remove the noise induced by the phase offsets without hardware modification. Existing techniques include multiplying one stream by the complex conjugate of the other (CM) [25], and dividing one stream by the other (CSI ratio) [22]. CM leaves some residue of the noise while the CSI ratio loses its scale. Therefore, we apply both techniques on X, creating X_{CM} and X_R, respectively. Note that these processes collapse X into one stream.

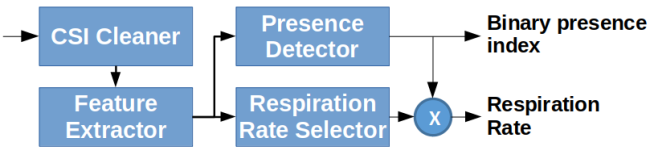

Fig. 3: The architecture of PresSense.

To filter out high frequencies that are unrelated to human respiration, we apply the Savitzky-Golay Filter (SGF), as in [21], [22], which fits successive subsequences of the CSI measured within some time window t_w, with polynomials of a low-degree d using linear least squares. We use $t_w = 1$ second and $d = 3$ in our experiment, creating X'_{CM} and X'_R from X_{CM} and X_R, respectively.

The subtle periodic respiration pattern is better captured in X'_R than in X'_{CM} as CM is more vulnerable to noise. To further reveal these patterns in X'_R, we adopt the method from [22] that projects each the complex CSI subcarrier to real and applies autocorrelation on these projections, creating Y'_R. The projection axes are chosen such that the respiration signal is more emphasized based on the Respiration-to-Noise-Ratio (RNR) metric. RNR, as proposed by [26], defines the ratio of the respiration power over the overall power and it is computed using Fast Fourier Transform (FFT). The autocorrelation function measures how similar a signal is to a delayed version of itself. When applied to a periodic signal, the autocorrelation is also periodic with the same period [27]. Y'_R is often smoother and easier to extract the peaks than X'_R. Finally, all X_{CM}, X_R, X'_{CM}, X'_R and Y'_R are passed to the Feature Extractor.

B. Feature Extractor

There exist various WiFi features to describe the signal patterns and the activity in the sensing area. This module extracts features inspired from [7], [21], [22], [28] and our novel respiration sensing feature PDH. Note that we have also tested other features that are excluded from this paper and empirically choose the ones presented below. Table I shows the complete list of features that we pass to the subsequent modules.

1) Variance and magnitude (VM): Empirically, the variance and magnitude of the CSI capture the dynamic and static components in the multipath propagation. The variance is expected to increase according to the amount of motions and the magnitude is expected to change depending on the configuration and the objects/people present in the sensing area. For each X_{CM} and X'_{CM}, we extract the median variance across each CSI subcarrier (σ_{CM} and σ'_{CM}) and the median magnitude ($|X_{\text{CM}}|$ and $|X'_{\text{CM}}|$). We also extract $\Delta\sigma_{\text{CM}} = \sigma_{\text{CM}} - \sigma'_{\text{CM}}$ and $\Delta|X_{\text{CM}}| = |X_{\text{CM}}| - |X'_{\text{CM}}|$, which capture how much of σ_{CM} and $|X_{\text{CM}}|$ are related to the filtered out high frequencies.

2) Principal component analysis (PCA): If the variation of the CSI subcarriers is highly correlated due to some underlying factor, then PCA can be applied to evaluate such correlation. We apply PCA across the subcarriers and extract the sum of the explained variance of the first 3 components (PCA3). PCA3 value for empty AOI is expected to be lower than for occupied AOI.

3) Mean Doppler spectrum (MDS): The motion of the human chest can create Doppler frequency shifts (DFS) extractable from the CSI using FFT. MDS captures the strength of DFS averaged over all CSI subcarriers. When there is no motion, a narrow and sharp peak at 0Hz in the MDS is expected. When motion is present, it may have a wider peak as in the example in Figure 4(a). This quality of MDS can be measured using the Spectral Centroid (SC) and Spectral Spread (SS) as defined in [28].

4) Respiration-to-Noise-Ratio and autocorrelation (RNRxA): Since Y'_R captures the periodicity in the CSI, the state of the art respiration sensing system, FarSense [22], combines Y'_R with relatively high RNR into one signal by weighted averaging based on their RNR, and use the time of the first peak to estimate the respiration rate (BR'_R). See example in Figure 4(b). Our Feature Extractor extracts the mean RNR of Y'_R ($\text{B}\mu'_R$) the autocorrelation value (BP'_R) of the first peak that derived BR'_R and the prominence (BPP'_R) of that peak. The peak prominence measures how much the peak stands out relative to the sounding values. When respiration is present, the first peak is expected to be positive and prominent.

5) Power Spectral Density (PSD): An alternative to RNR, the portion of Y'_R to use for rate estimation can be selected using PSD, which describes the power of the frequencies present in the signals. We adopt the method from [21], which selects the subcarrier with the maximum PSD power within the valid respiration rate range, and uses the mean peak distance to estimate the respiration rate. Our Feature Extractor extracts the estimated rate (PR), the standard deviation of the power from the selected subcarrier ($\text{PP}\sigma$), the latter's maximum power (PP) and the frequency corresponding to the maximum power in the PSD (PF).

6) Peak Distance Histogram (PDH): BR'_R, as reported by the state-of-the-art respiration sensing method [22], is derived using the weighted average of multiple signals which can be constructive or destructive depending on their in-phase or out-of-phase relationship. This can cause a major problem in a noisy environment with multiple respiration sources outside of the AOI. In our experiment, we have found that PR'_R, derived from the subcarrier with the largest PSD power in Y'_R, often gives us a higher accuracy than BR'_R. However, it is possible that the signal with the largest power is not fully descriptive of the ground truth due to possible stronger respiration outside of the AOI or the small bias induced by the SGF [29]. In this case, we can consider the respiration signal that is the most frequently observed in Y'_R. This leads us to develop PDH.

PDH which takes input Y'_R, uses a peak detection algorithm with minimum peak distance of 1.5 seconds, and counts the frequency of time distances between consecutive peaks that correspond to at most 2 breaths away from the valid respiration range (8 to 39 bpm). We use a bin step of $\delta = 1/150$, giving us $n_b = 4651$ frequency bins. Given n_p peak time distances $[p_1, \ldots, p_{n_p}]$ in seconds, the value for each bin is defined as $b_i = \sum_{j=1}^{n_p} b_{i,j}$ where $i \in \{1, \ldots, n_b\}$,

$$b_{i,j} = \log\big(\min\{|f_i - 1/p_j|, 1 - \epsilon\} + \epsilon\big), \tag{3}$$

$$f_i = (i-1)\delta + f_0, \tag{4}$$

where $f_0 = 8/60$ is the smallest respiration frequency and $\epsilon = 1\text{e}{-10}$ to avoid 0 in the logarithm. Different

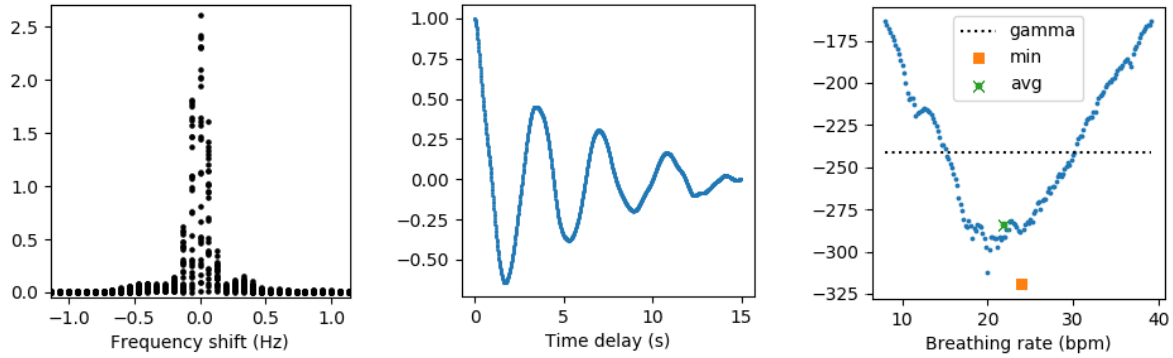

(a) Mean Doppler Spectrum (MDS).

(b) Autocorrelation with the first peaks at around 3 sec, giving us a respiration rate of $60/3 = 20$ bpm.

(c) Peak Distance Histogram (PDH) with the minimum value around 24 bpm (HMR'_R), and the weighted average around 22 bpm (HR'_R).

Fig. 4: Example of MDS, autocorrelation and PDH when someone is present in the AOI.

from traditional histograms, Equation (3) allows us to count each p_j in multiple bins with appropriate weight, which is more robust to noise. The min operation bounds the values below 0. Then, we filter out the bins with value larger than $\gamma = (\max_i(b_i) + \min_i(b_i))/2$ and use the average frequency weighted by the bin value (HR'_R) as the estimate the respiration rate:

$$\text{HR}'_R = 60 \sum_{i=1}^{n_b} f_i w_i, \tag{5}$$

$$w_i = \begin{cases} \frac{\gamma - b_i}{\sum_{j=1}^{n_b}(\gamma - b_j)} & \text{if } b_i < \gamma \\ 0 & \text{otherwise} \end{cases}, \tag{6}$$

where w_i is the normalized weight according to the bin value. We also extract descriptors of the PDH, namely, the weighted bin average ($\text{H}b'_R$), the weighted frequency standard deviation ($\text{H}\sigma'_R$), as defined below:

$$\text{H}b'_R = \sum_{i=1}^{n_b} b_i w_i, \tag{7}$$

$$\text{H}\sigma'_R = \sqrt{\sum_{i=1}^{n_b} \left(f_i - \text{HR}'_R/60\right)^2 w_i}, \tag{8}$$

and the standard deviation of $\{\text{HR}'_R, \text{HMR}'_R\}$ ($\text{HR}\sigma'_R$) where HMR'_R is the rate computed using the frequency corresponding to the minimum bin value. In addition, we extract the standard deviation of all peak distances in bpm ($\text{HP}\sigma'_R$). Figure 4(c) show an example of PDH.

We believe that PDH is a generic WiFi feature and can be easily adapted to different frequency ranges by tuning δ and f_0. It can be integrated into filtering algorithms and used in applications for analyzing noisy periodic patterns.

C. Presence Detector

Table I lists the features that we pass to our Presence Detector. The latter concatenates these features across k consecutive and overlapping CSI sequences of length n and uses Random Forest Classifier with 100 instances to distinguish between an occupied and empty AOI. In our experiment, $k = 6$, $n = 15r$ and the overlap is $n - 2r$, where r is the sampling rate. This allows us to give more weight to feature values that are common across the k sequences, resulting in higher robustness to noise.

D. Respiration Rate Selector

Table I lists the features that we pass to our Respiration Rate Selector. Our estimated respiration rate is set to PR'_R if $\text{SS}_{\text{CM}} > 5$, $\text{SS}'_{\text{CM}} > 2$, $\text{SC}_{\text{CM}} > 2$, $\text{SC}'_{\text{CM}} > 1$, $|X_{\text{CM}}| < 1$ or $|X'_{\text{CM}}| < 1$. Otherwise, it is set to HR'_R. Empirically, the first four conditions test if there are many respiration sources [28] and the last two test if many WiFi propagation paths are blocked by, for example, the human body standing near the Line of Sight (LoS). Note that these rules are manually tuned and may differ for different environments and WiFi devices. Finally, if the estimated respiration rate is not within the valid respiration range, we set it to 0.

IV. Evaluation

We implemented PresSense in Python and evaluated it in a real-world scenario in non-real-time as a proof of concept.

A. Experiment Setup

Our AOI is an office room with two tables and a chair, shown in Fig 5. We created ambient WiFi signals in the room by pinging a TP-Link AC1750 WiFi router with a Dell Latitude E7440 laptop, on a 2.4GHz WiFi channel. The pinging rate was $r = 100$ samples per second. We installed the Linux CSI Tool [30] on the laptop to extract WiFi CSI.

B. Data Collection

We collected data on 6 participants (labelled as ID1 to ID6). The statistics of the participants are presented in Fig. 6. We asked each participant to stand at each of the positions (P1 to P4) and to report to us the number of breaths taken during 30 seconds. This process is repeated for three different facing directions and two door states (open and closed).

Module	Input Features		Category
PD	σ_{CM}	Median CSI variance	
both	$\lvert X_{\text{CM}}\rvert$	Median CSI magnitude	
RRS	$\lvert X'_{\text{CM}}\rvert$	Median CSI magnitude of the low frequencies	VM
PD	$\Delta\sigma_{\text{CM}}$	CSI variance related to the high frequencies	
PD	$\Delta\lvert X_{\text{CM}}\rvert$	CSI magnitude related to the high frequencies	
PD	$\text{PCA3}'_{\text{CM}}$	Sum of explained variance of the top 3 principal components of the low frequencies	PCA
PD	$\text{PCA3}'_{R}$	Sum of explained variance of the top 3 principal components of the low frequencies in the CSI ratio	
RRS	SC_{CM}	Spectrum Center	
RRS	SC'_{CM}	Spectrum Center of the low frequencies	
both	SS_{CM}	Spectrum Spread	MDS
RRS	SS'_{CM}	Spectrum Spread of the low frequencies	
PD	SS_{R}	Spectrum Spread in the CSI ratio	
PD	SC'_{R}	Spectrum Center of the low frequencies in the CSI ratio	
PD	SS'_{R}	Spectrum Spread of the low frequencies in the CSI ratio	
PD	$\text{B}\mu'_{R}$	Mean RNR	
PD	BPP'_{R}	Prominence of the first peak after applying autocorrelation and combining the subcarriers	RNRxA
PD	BP'_{R}	Value of the first peak after applying autocorrelation and combining the subcarriers	
PD	PF'_{CM}	Frequency with the max power in the PSD	
PD	PF'_{R}	Frequency with the max power in the PSD computed from the CSI ratio projections	PSD
PD	PP'_{R}	Maximum power in the PSD computed from the CSI ratio projections	
PD	$\text{PP}\sigma'_{R}$	STD of the power in the PSD computed from the CSI ratio projections	
RRS	PR'_{R}	Respiration rate estimated from the subcarrier with the largest power computed from the CSI ratio projections	
PD	Hb'_{R}	Weighted bin average in PDH	
PD	$\text{H}\sigma'_{R}$	Weighted frequency standard deviation in PDH	PDH
PD	HMR'_{R}	STD of detectable respiration rates using the minimum or weighted average of the bins in PDH	
PD	$\text{HP}\sigma'_{R}$	STD of the peak distances in bpm	
RRS	HR'_{R}	Respiration rate estimated using PDH	

TABLE I: Input feature list for each downstream module: Presence Detection (PD) and Respiration Rate Selector (RRS).

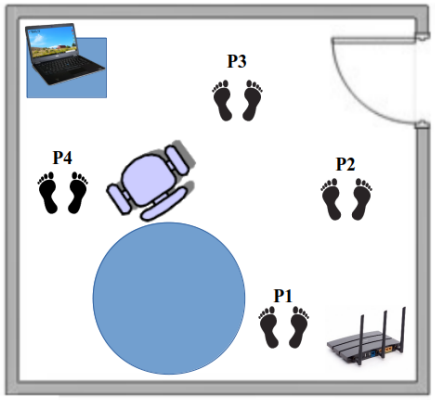

Fig. 5: Experiment Setup.

In total, we collected $432K$ CSI measurements with the participants and $144K$ with the room emptied. We treated the data from ID1 and $84K$ of the data from the empty room as the training set, and considered the rest as the testing set.

Note that, during our experiments, there were other people outside the room working on their daily jobs. It is also possible that the chair slightly changes position by accident. Although our dataset is noisier compared to those collected under more controlled environments [21], [22], it is more representative of real-world scenarios.

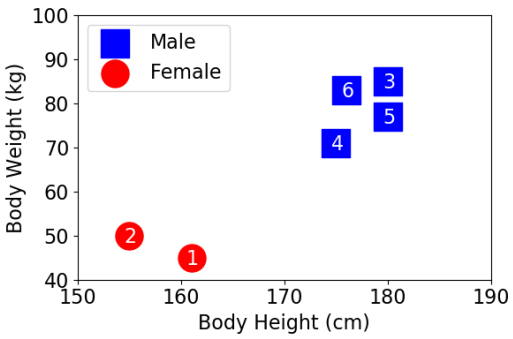

Fig. 6: Weights and heights of participants.

C. Respiration sensing

1) Methods Compared: We compared the following respiration sensing methods.

- **FullBreathe** [21] employed PSD to find the respiration signal with the largest power in the filtered CSI using CM and SGF.
- **FarSense** [22] filtered the CSI using CSI ratio and SGF, and estimate the respiration rate using the first peak in the weighted average of the autocorrelations of signals with large RNR.
- **PresSense**, the method proposed in this paper.

2) Accuracy: We compared the Mean Absolute Errors (MAEs) of respiration sensing in Table II. When evaluated on all the testing data, PresSense achieved a MAE of 0.5 bpm which outperformed FullBreathe and FarSense by 2.5

times and 1.8 times, respectively. In particular, the improvements were 1.7 times and 1.4 times, respectively, when the room was occupied. When the room was empty, while the proposed PresSense detected no respiration, FullBreathe and FarSense sometimes falsely recognized noise sources (e.g., human motions and respiration outside the room) as valid respiration. Therefore, they performed poorly when no one was in the room.

	MAE (bpm)		
	FullBreathe	FarSense	PresSense
All Testing Data	13.1	9.2	**5.1**
Occupied Room	10.3	8.2	**5.9**
Empty Room	29.7	15.4	**0.0**

TABLE II: MAEs of respiration sensing.

In fact, in the occupied room scenario, FullBreathe and FarSense were also sensitive to the respiration/motions outside the AOI. We further analyzed the MAEs at different positions when the room was occupied. From Fig. 7, we confirmed that PresSense performed constantly better than the other two methods across different positions.

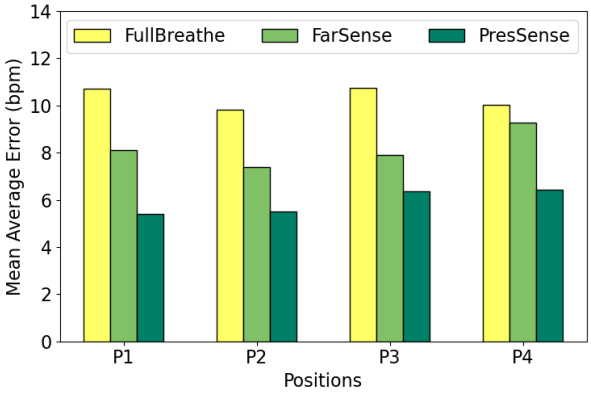

Fig. 7: MAEs of respiration rates at different positions.

3) Ablation Study: Since PresSense borrowed some features from FullBreathe (PSD) and FarSense (RNRxA), we conducted an ablation study to better understand each of them. In Table III, we listed the MAE of respiration sensing on occupied room data, using different features. Comparing row 1 and row 2, we found that using the PSD to select the best signal in Y'_R achieve better results than combining multiple signals in Y'_R. Comparing row 1 and row 3, we found that adding our proposed PDH feature improved the state of the art, FarSense, by up to 23.5%. Comparing row 2 and row 3, we found that PSD and PDH were two complementary features. While PSD achieving smaller errors at some positions, PDH obtained better results at others. Thereby, in the last row, by integrating all these features, PresSense outperformed others.

4) Robustness to Different Users: Different people have different body shapes and unique respiration patterns. These factors may affect the accuracy of the estimated respiration rates. Thus, we further evaluated the methods on different participants to see if they were robust to user diversity. Fig. 8 presented the MAEs of respiration rates across different participants. Among the three methods presented, FullBreathe had the most unstable performance, with its MAE ranging from 3.5 bpm for ID2 to 17.2 bpm for ID4. FarSense's performance also varied a lot. It could be the worst method for ID1 to ID3, and at the same time could outperform the other two for ID4. On the contrary, PresSense remained the best method for all participants (except ID4). Hence, we concluded that PresSense provided the most robust respiration sensing.

Features			MAE (bpm)			
PSD (FullBreathe)	RNRxA (FarSense)	PDH	P1	P2	P3	P4
×	◯	×	8.1	7.4	7.9	9.3
◯	◯	×	6.6	6.5	7.6	6.9
×	◯	◯	6.2	5.7	7.0	7.5
◯	◯	◯	**5.4**	**5.5**	**6.3**	**6.4**

TABLE III: MAEs of respiration rate using different features.

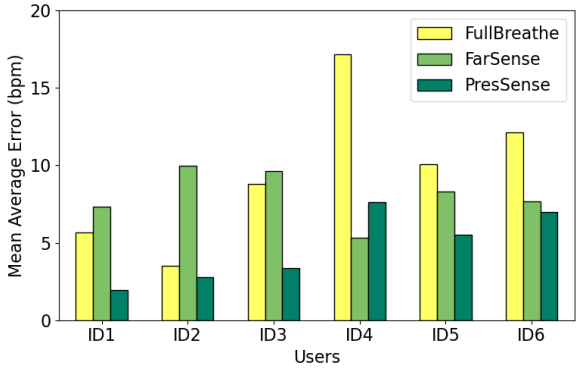

Fig. 8: MAEs of respiration rates for different users.

D. Presence Detection

1) Methods Compared: Since existing respiration sensing methods did not provide an explicit presence detection service, we evaluated PresSense's presence detection against the following methods.

- **MoFi** [31] provided a motion detector based on thresholds of CSI variance of variances (VoV).
- **AutoFi** [6] was a fingerprint-based indoor localization method. In our experiments, AutoFi used the WiFi fingerprints of from the same training set to train a binary presence detector.
- **PresSense**, the method proposed in this paper.

2) Accuracy: Table IV presents the accuracy of presence detection. MoFi was essentially a motion detector instead of a presence detector. As a result, it achieved an acceptable performance in empty-room scenarios, and yet experienced lots of false negatives in the occupied-room scenarios. AutoFi outperformed MoFi with its binary presence classifier in the occupied-room scenarios. However, it was overfit to ID1's

data (the training data), and thus performed poorly in the empty-room scenarios. By learning from more generic user-independent features, the classifier in PresSense achieved the highest accuracy in all scenarios.

	Detection Accuracy		
	MoFi	AutoFi	PresSense
All Testing Data	18.0%	70.1%	**92.4%**
Occupied Room	7.5%	73.3%	**91.1%**
Empty Room	81.0%	50.8%	**100.0%**

TABLE IV: Accuracy of presence detection.

3) Ablation Study: PresSense obtained high presence detection accuracy by integrating a diversity of features. Next, we conducted an ablation study on these features to illustrate their contributions. Table V summarizes the presence detection accuracy using different sets of features. In row 1 and row 2, we could see that, when the room was empty, PDH related features performed better than VM related features. The results were reversed when someone was in the room. Comparing row 1 and row 3, it was confirmed that using multiple features that are not specifically analyzing respiration patterns provided higher accuracy than using just one. Comparing row 3 and row 4, it was confirmed that adding information about respiration from PDH improves the accuracy when someone was in the room. From row 1 to row 7, we can see that integrating different features allowed us to absorb their advantages. The more features we used, the better the performance we obtained. Comparing row 6 with row 7, we found that the proposed PDH related features helped further increase the accuracy.

V. Related Work

In this section, we discuss WiFi-based approaches for respiration rate sensing, presence detection and motion detection.

A. Respiration rate sensing

One of the main challenges in using CSI is to extract consistent consecutive measurements since commodity WiFi devices suffer from several time-varying phase offsets [32]. Previously, many respiration detection systems [12]–[15], were based only on the CSI amplitude. X. Wang *et al.* developed phase-based systems, TensorBeat [16] and PhaseBeat [17], using the phase difference between two antennas to cancel out the offsets, giving that the offsets are the same across the same WiFi card. However, this method can be constructive or destructive depending on whether the two signals are in-phase or out-of-phase. D. Zhang *et al.* also proposed a phase-based system, BreathTrack [18], leveraging the conjugate multiplication (CM) of the CSI from two antennas to remove the offset, a phase cleaning method proposed by [25]. The above-mentioned respiration rate sensing systems are all based on detecting a periodic pattern in either the CSI amplitude or the CSI phase, but they are oblivious to why different human locations and orientations can lead to drastically different waveforms.

H. Wang *et al.* [19] introduced a theoretical model based on the Fresnel Zone (FZ) to explain an alternating sensitivity of CSI amplitude and CSI phase across the sensing area. P. Wang *et al.* developed TinySense [20] using multiple transceiver pairs to increase the density of the Fresnel Zone and hence, enhance the sensitivity of the CSI amplitude. Y. Zheng *et al.* [21] demonstrated the complementary property of CSI amplitude and phase. Their proposed system, FullBreathe, estimates a respiration rate from either the CSI amplitude or phase, resulting in a consistent detection across the sensing area. Recent work by Y. Zheng *et al.* [22] introduced CSI ratio to remove the phase offset. They demonstrated that the noise present in the raw CSI can be mostly cancelled out by the division between two antennas, and hence, the resulting CSI ratio is more sensitive to fine-grained subtle movement. Their proposed system, FarSense, made a significant improvement in the sensing range.

The aforementioned systems operate in relatively quiet environments with the assumption that there is one and only one respiration source. In our work, we relax this assumption by combining presence and respiration rate sensing into one system, improving its robustness to noise.

B. Presence and Motion detection

Presence/motion detection has been utilized as the trigger of succeeding services such as respiration detection, localization or activity recognition. For example, X. Chen *et al.* in [6] developed a CSI-variance based motion detection method, which was used to trigger the update of their WiFi localization system AutoFi. W. Xi *et al.* in [33] monitored the Percentage of nonzero Elements (PEM) in the CSI matrix, and used this metric to infer the number of people in the area of interest. S. Domenico *et al.* in [28] estimated the presence and the crowd number by extracting spectral descriptors from the Mean Doppler Spectrum (MDS) of the CSI, using a Naive Bayes classifier. K. Qian *et al.* in [34] directly used raw CSI magnitudes and phases to train an SVM, which detected the presence of moving humans.

The errors in detecting human presence and/or motion would largely affect the quality of the succeeding services. However, such an error propagation has not been extensively analyzed prior to this work. By incorporating a robust presence detector in the design, PresSense further improves the accuracy of respiration rate sensing.

VI. Conclusion

Passive respiration sensing via ambient WiFi signals provides a new possibility for robots to sense human presence and their state of activity. However, the subtle respiration pattern is easily overwhelmed by noise and existing systems have limited performance in real-world scenarios. By combining presence detection and respiration sensing, and by using a new WiFi feature, Peak Distance Histogram (PDH), for counting the occurrence of periodic patterns, our proposed PresSense greatly enhances the sensing accuracy and robustness in noisy environments, outperforming the state of the art by at least 28.0% for respiration rate

	Feature Category						Presence Accuracy	
	VM	PDH	PCA	MDS	PSD	RNRxA	Occupied Room	Empty Room
1	◯	×	×	×	×	×	62.7%	63.5%
2	×	◯	×	×	×	×	35.7%	88.9%
3	◯	×	◯	◯	×	×	84.1%	98.4%
4	◯	◯	◯	◯	×	×	89.4%	98.4%
5	◯	◯	◯	◯	◯	×	88.3%	100.0%
6	◯	×	◯	◯	◯	◯	87.5%	100.0%
7	◯	◯	◯	◯	◯	◯	**91.1%**	**100.0%**

TABLE V: Acurracy of presence detection using different features.

estimation and at least 17.8% for presence detection in our experiment. We believe that our improvements in WiFi-based passive respiration sensing can further help in enabling new sensing technologies for human-robot interactions. Future work includes presence and respiration sensing for multiple person in an AOI, and generalization to different AOIs.

REFERENCES

[1] Zimo Li, Prakruti C. Gogia, and Michael Kaess. Dense surface reconstruction from monocular vision and lidar. In *ICRA*, pages 6905–6911. IEEE, 2019.

[2] Sarah H. Cen and Paul Newman. Radar-only ego-motion estimation in difficult settings via graph matching. In *ICRA*, pages 298–304. IEEE, 2019.

[3] Francois Robert Hogan, Maria Bauzá, Oleguer Canal, Elliott Donlon, and Alberto Rodriguez. Tactile regrasp: Grasp adjustments via simulated tactile transformations. In *IROS*, pages 2963–2970. IEEE, 2018.

[4] Keisuke Koyama, Kenichi Murakami, Taku Senoo, Makoto Shimojo, and Masatoshi Ishikawa. High-speed, small-deformation catching of soft objects based on active vision and proximity sensing. *IEEE Robotics and Automation Letters*, 4(2):578–585, 2019.

[5] Xingxing Zuo, Patrick Geneva, Woosik Lee, Yong Liu, and Guoquan Huang. Lic-fusion: Lidar-inertial-camera odometry. In *IROS*, pages 5848–5854. IEEE, 2019.

[6] Xi Chen, Chen Ma, Michel Allegue, and Xue Liu. Taming the inconsistency of wi-fi fingerprints for device-free passive indoor localization. In *INFOCOM*, pages 1–9. IEEE, 2017.

[7] Xi Chen, Hang Li, Chenyi Zhou, Steve Liu, Di Wu, and Gregory Dudek. Fido: Ubiquitous fine-grained wifi-based localization for unlabelled users via domain adaptation. In *WWW*, pages 1–10. ACM, 2020.

[8] Joydeep Biswas and Manuela M. Veloso. Wifi localization and navigation for autonomous indoor mobile robots. In *ICRA*, pages 4379–4384. IEEE, 2010.

[9] Manikanta Kotaru, Kiran Raj Joshi, Dinesh Bharadia, and Sachin Katti. Spotfi: Decimeter level localization using wifi. In *SIGCOMM*, pages 269–282. ACM, 2015.

[10] Kun Qian, Chenshu Wu, Yi Zhang, Guidong Zhang, Zheng Yang, and Yunhao Liu. Widar2.0: Passive human tracking with a single wi-fi link. In *MobiSys*, pages 350–361. ACM, 2018.

[11] Yue Zheng, Yi Zhang, Kun Qian, Guidong Zhang, Yunhao Liu, Chenshu Wu, and Zheng Yang. Zero-effort cross-domain gesture recognition with wi-fi. In *MobiSys*, pages 313–325. ACM, 2019.

[12] Xuefeng Liu, Jiannong Cao, Shaojie Tang, and Jiaqi Wen. Wi-sleep: Contactless sleep monitoring via wifi signals. In *RTSS*, pages 346–355. IEEE Computer Society, 2014.

[13] Jian Liu, Yan Wang, Yingying Chen, Jie Yang, Xu Chen, and Jerry Cheng. Tracking vital signs during sleep leveraging off-the-shelf wifi. In *MobiHoc*, pages 267–276. ACM, 2015.

[14] Xuefeng Liu, Jiannong Cao, Shaojie Tang, Jiaqi Wen, and Peng Guo. Contactless respiration monitoring via off-the-shelf wifi devices. *IEEE Trans. Mob. Comput.*, 15(10):2466–2479, 2016.

[15] Chenshu Wu, Zheng Yang, Zimu Zhou, Xuefeng Liu, Yunhao Liu, and Jiannong Cao. Non-invasive detection of moving and stationary human with wifi. *IEEE Journal on Selected Areas in Communications*, 33(11):2329–2342, 2015.

[16] Xuyu Wang, Chao Yang, and Shiwen Mao. Tensorbeat: Tensor decomposition for monitoring multiperson breathing beats with commodity wifi. *ACM TIST*, 9(1):8:1–8:27, 2017.

[17] Xuyu Wang, Chao Yang, and Shiwen Mao. Phasebeat: Exploiting CSI phase data for vital sign monitoring with commodity wifi devices. In *ICDCS*, pages 1230–1239. IEEE Computer Society, 2017.

[18] Dongheng Zhang, Yang Hu, Yan Chen, and Bing Zeng. Breathtrack: Tracking indoor human breath status via commodity wifi. *IEEE Internet of Things Journal*, 6(2):3899–3911, 2019.

[19] Hao Wang, Daqing Zhang, Junyi Ma, Yasha Wang, Yuxiang Wang, Dan Wu, Tao Gu, and Bing Xie. Human respiration detection with commodity wifi devices: do user location and body orientation matter? In *UbiComp*, pages 25–36. ACM, 2016.

[20] Pei Wang, Bin Guo, Tong Xin, Zhu Wang, and Zhiwen Yu. Tinysense: Multi-user respiration detection using wi-fi CSI signals. In *Healthcom*, pages 1–6. IEEE, 2017.

[21] Youwei Zeng, Dan Wu, Ruiyang Gao, Tao Gu, and Daqing Zhang. Fullbreathe: Full human respiration detection exploiting complementarity of CSI phase and amplitude of wifi signals. *IMWUT*, 2(3):148:1–148:19, 2018.

[22] Youwei Zeng, Dan Wu, Jie Xiong, Enze Yi, Ruiyang Gao, and Daqing Zhang. Farsense: Pushing the range limit of wifi-based respiration sensing with CSI ratio of two antennas. *IMWUT*, 3(3):121:1–121:26, 2019.

[23] Belal Korany, Chitra R. Karanam, Hong Cai, and Yasamin Mostofi. Xmodal-id: Using wifi for through-wall person identification from candidate video footage. In *MobiCom*, pages 36:1–36:15. ACM, 2019.

[24] IEEE. IEEE 802.11n standard.

[25] Xiang Li, Daqing Zhang, Qin Lv, Jie Xiong, Shengjie Li, Yue Zhang, and Hong Mei. Indotrack: Device-free indoor human tracking with commodity wi-fi. *IMWUT*, 1(3):72:1–72:22, 2017.

[26] Zhihong He, Lingchao Guo, Zhaoming Lu, Xiangming Wen, Wei Zheng, and Shuang Zhou. Contact-free in-home health monitoring system with commodity wi-fi. In *ICC Workshops*, pages 1–6. IEEE, 2019.

[27] George EP Box, Gwilym M Jenkins, Gregory C Reinsel, and Greta M Ljung. *Time series analysis: forecasting and control*. John Wiley & Sons, 2015.

[28] Simone Di Domenico, Giovanni Pecoraro, Ernestina Cianca, and Mauro De Sanctis. Trained-once device-free crowd counting and occupancy estimation using wifi: A doppler spectrum based approach. In *WiMob*, pages 1–8. IEEE Computer Society, 2016.

[29] Jin Chen, Per Jönsson, Masayuki Tamura, Zhihui Gu, Bunkei Matsushita, and Lars Eklundh. A simple method for reconstructing a high-quality ndvi time-series data set based on the savitzky–golay filter. *Remote sensing of Environment*, 91(3-4):332–344, 2004.

[30] Daniel Halperin, Wenjun Hu, Anmol Sheth, and David Wetherall. Tool release: Gathering 802.11n traces with channel state information. *SIGCOMM Comput. Commun. Rev.*, 41(1):53–53, 2011.

[31] Xi Chen, Hang Li, Chenyi Zhou, Steve Liu, and Gregory Dudek. Mofi: Environment-independent device-free human motion detection via wifi. In *RTSS@Work*, pages 1–2. IEEE, 2019.

[32] Yaxiong Xie, Zhenjiang Li, and Mo Li. Precise power delay profiling with commodity wifi. In *MobiCom*, pages 53–64. ACM, 2015.

[33] Wei Xi, Jizhong Zhao, Xiang-Yang Li, Kun Zhao, Shaojie Tang, Xue Liu, and Zhiping Jiang. Electronic frog eye: Counting crowd using wifi. In *INFOCOM*, pages 361–369. IEEE, 2014.

[34] Kun Qian, Chenshu Wu, Zheng Yang, Yunhao Liu, Fu-gui He, and Tianzhang Xing. Enabling contactless detection of moving humans with dynamic speeds using CSI. *ACM Trans. Embedded Comput. Syst.*, 17(2):52:1–52:18, 2018.